
Operator Learning Using Weak Supervision from Walk-on-Spheres

Hrishikesh Viswanath^{*1} Hong Chul Nam^{*2} Xi Deng³ Julius Berner⁴³ Anima Anandkumar³ Aniket Bera¹

Abstract

Training neural PDE solvers is often bottlenecked by expensive data generation or unstable physics-informed neural network (PINN) involving challenging optimization landscapes due to higher-order derivatives. To tackle this issue, we propose an alternative approach using Monte Carlo approaches to estimate the solution to the PDE as a stochastic process for weak supervision during training. Leveraging the Walk-on-Spheres method, we introduce a learning scheme called *Walk-on-Spheres Neural Operator (WoS-NO)* which uses weak supervision from WoS to train any given neural operator. We propose to amortize the cost of Monte Carlo walks across the distribution of PDE instances using stochastic representations from the WoS algorithm to generate cheap, noisy, estimates of the PDE solution during training. This is formulated into a data-free physics-informed objective where a neural operator is trained to regress against these weak supervisions, allowing the operator to learn a generalized solution map for an entire family of PDEs. This strategy does not require expensive pre-computed datasets, avoids computing higher-order derivatives for loss functions that are memory-intensive and unstable, and demonstrates zero-shot generalization to novel PDE parameters and domains. Experiments show that for the same number of training steps, our method exhibits up to $8.75\times$ improvement in L_2 -error compared to standard physics-informed training schemes, up to $6.31\times$ improvement in training speed, and reductions of up to $2.97\times$ in GPU memory consumption. We present the code at <https://github.com/neuraloperator/WoS-NO>

1. Introduction

Partial Differential Equations (PDEs) are fundamental mathematical tools for modeling a wide range of physical, geo-

^{*}Equal contribution ¹Purdue University, USA ²ETH Zurich, Switzerland ³California Institute of Technology, USA ⁴NVIDIA, USA. Correspondence to: Hrishikesh Viswanath <hviswan@purdue.edu>.

Preprint. March 4, 2026.

metric, and engineering systems. These equations describe how quantities vary across a domain, with applications spanning diverse scientific fields. A common thread across these fields is the challenge of solving the governing PDEs, a task often complicated by the complex and irregular geometries of the underlying domains.

Traditional methods for solving PDEs on complex geometries often fall into two broad categories: grid-based methods and grid-free approaches. Grid-based methods, such as finite difference method (FDM), finite volume method (FVM), and finite element method (FEM), discretize the domain into a grid or mesh and numerically solve PDEs over those partitions. Although these methods are highly accurate and widely used, their performance depends on the level of discretization, and they can become computationally prohibitive for large-scale problems or domains with complex geometries. Moreover, when the meshes are highly irregular or faulty, with cracks and sliver faces, they require computationally expensive geometric healing before they can be used in FEM [7].

Among the class of grid-free numerical techniques are the Monte Carlo-based methods [37]. These methods express the solution of the PDE as the recursive path integral formulation and define a Monte Carlo estimator for the integral equation [23]. Among them, WoS is a notable technique that utilizes Brownian motion to estimate solutions to elliptic PDEs, notably the Poisson family of equations [30] by simulating random walks and their interaction with domain boundaries. WoS avoids the complexities associated with grid dependencies by computing point-wise estimates independently. While conventional solvers like FEM for Poisson equations are more efficient on simple domains, they encounter significant bottlenecks on complex, non-watertight geometries [38] where mesh generation, a prerequisite for FEM, is computationally expensive or prone to failure. By leveraging WoS, we bypass this volumetric meshing bottleneck entirely, enabling scalable learning directly on raw geometry. However, Monte Carlo methods suffer from slow convergence due to the high variance [38]. Achieving accurate estimates requires performing a large number of walks to reach the domain boundary, often of the order of 10^4 to 10^6 , to converge to the expected solution, leading to significant computational overhead.

Recent works have explored the integrations of neural networks with WoS to accelerate PDE solvers [21; 31]. These methods improve the solution accuracy, reduce the prediction variance, and amortize the prediction cost by using

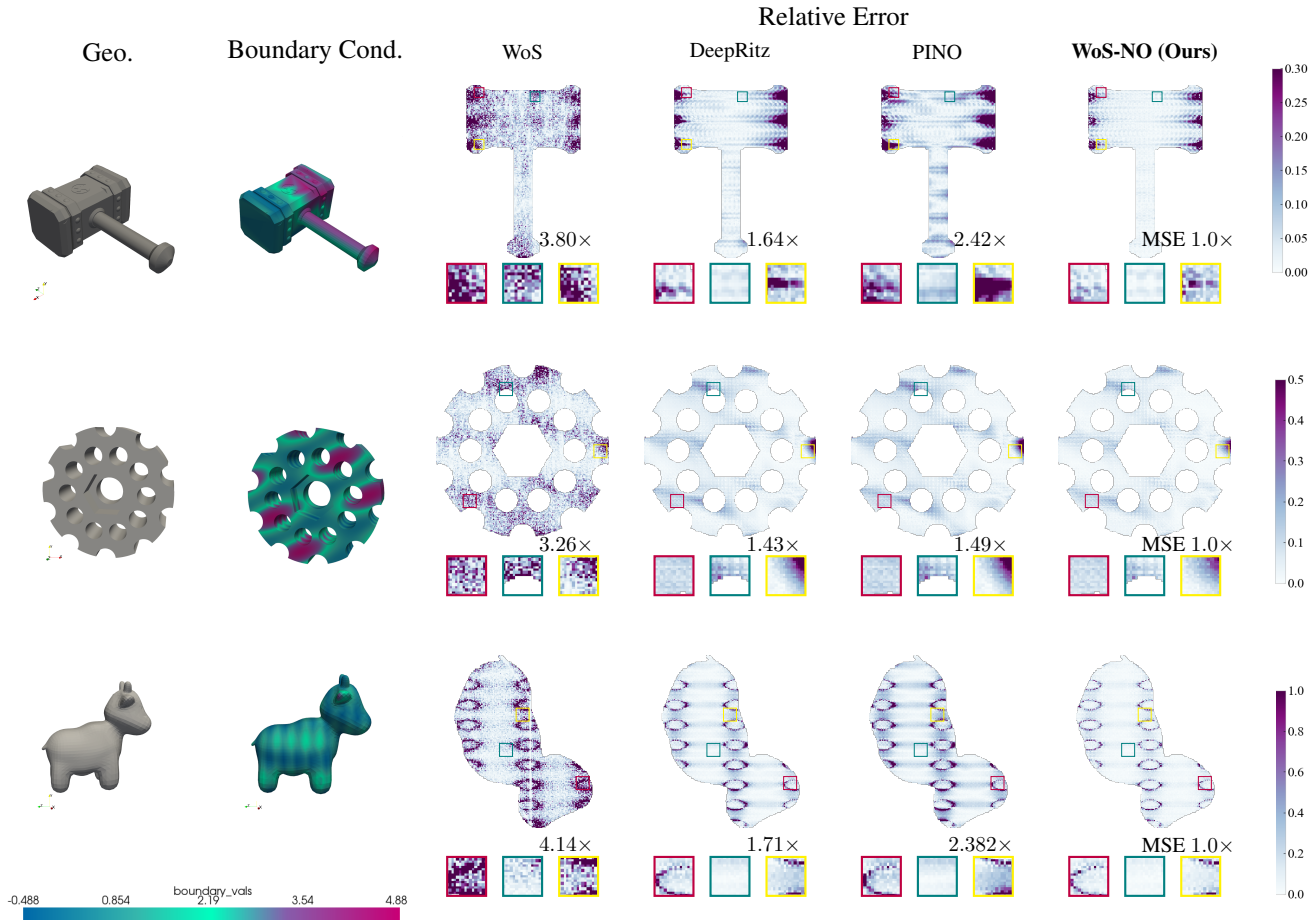


Figure 1. Given arbitrary, unseen input geometry and boundary conditions, we compare our method (WoS-NO) with WoS at equal execution time, and with DeepRitz and PINO at equal training time. We visualize the relative absolute error against the analytic solution of the PDE (the ground truth). We show that WoS-NO achieves the strongest performance (lowest relative error) in comparison with other baselines. During equal-time training, WoS-NO achieves $2.1\times$ overall improvement than PINO and $1.59\times$ than DeepRitz. During inference, WoS-NO achieves $3.73\times$ better performance than WoS under the same time constraint.

neural networks to learn from rough estimations from WoS, reducing the computational cost of explicitly simulating numerous random walks. However, such approaches are often parameterization-dependent: changes in the PDE parameters (e.g., source terms or coefficients) or variations in the domain geometry require the network to be retrained from scratch. This limitation hinders their ability to support zero-shot generalization on complex problems.

To this end, neural operators [2; 20; 22] offer a promising solution by directly learning the mapping between PDE coefficients and boundary functions to the solution, enabling zero-shot generalization to unseen geometries and PDEs. Such frameworks, however, rely on ground-truth solutions typically generated using FEM a priori. While these models achieve zero-shot generalization, the necessity of pre-computed training data introduces significant computational and memory overhead, particularly for large-scale meshes and high-dimensional problems. Extensions of physics-informed neural networks (PINNs) to neural operators (PINO) [24] aim to overcome the need for data by minimizing the PDE residual; however, this requires

(higher-order) derivative computations and suffers from optimization challenges [17], particularly when the training data are scarce.

Our Approach: We enable physics-informed training of neural operators without precomputed data by using stochastic estimates. In particular, we define a derivative-free regression objective using weak supervision from solution estimates generated with a minimal number of WoS trajectories. Due to the unbiasedness of the estimates as shown in [38], this simple and inexpensive regression objective still learns the groundtruth solution operator. Moreover, our strategy amortizes the cost of simulations across the family of PDEs, enabling the trained operator to infer solutions for unseen PDE instances and geometries in fractions of a second. While prior (neural) WoS approaches incur high costs to adapt to new problem instances, our operator learning framework achieves a constant inference cost for unseen PDE configurations with similar input-sizes. We demonstrate strong generalization, achieving $8.75\times$ improvement in L_2 -error compared to PINO while using $2.4\times$ less memory than PINO. Furthermore, we illustrate the zero-shot

generalization of our method for surface Laplace inpainting and fluid simulations.

Problem scope We focus our analysis on the family of linear elliptic PDEs, specifically Poisson families. While the WoS algorithm is classically rooted in this domain, limiting the scope to the Poisson family is driven by two factors: geometric robustness and computational ubiquity. Solving Poisson-type equations is a computational bottleneck in several engineering and biological applications. Stochastic methods for these equations have been successfully deployed in molecular dynamics [27], electrostatics for integrated circuit design [11; 18; 33], and flow in porous media [10]. Furthermore, recent advances leverage similar harmonic field formulations for autonomous robotic exploration in unknown environments [15], robust biharmonic skinning in computer graphics [8], and modeling protein drift-diffusion dynamics in curved cell membranes [29; 42].

Moreover, while we utilize the Poisson formulation to establish the paradigm of weakly-supervised neural operators, the underlying stochastic framework can be extended to broader PDE families. The Monte Carlo methodology has already been adapted to solve transient diffusion problems [41], reaction-diffusion equations [35], the Lamé equation for elasticity [1], and electron transport [13]. More recently, these methods have extended to non-linear advection-dominated regimes, including the Navier-Stokes and Burgers equations [36], as well as turbulent vector field representation [14]. By validating our neural operator framework on the foundational Poisson family, we provide the necessary groundwork for a learning paradigm that can eventually extend to these advanced stochastic estimators as they mature.

We empirically validate the advantages of using Monte-Carlo methods like WoS by training on non-watertight meshes from the ShapeNet dataset, a regime where traditional solvers typically require extensive manual repair, as shown in Figure 1. Furthermore, the Poisson equation serves as a critical computational primitive within broader non-linear physics, most notably as the pressure projection step in incompressible fluid dynamics [12]. Therefore, validating our framework on this family provides a verifiable pathway toward accelerating the internal loops of higher-order non-linear solvers, which we discuss in Section 5.4, where we consider 2 such cases: biharmonic image inpainting and Karman Vortex experiment [12].

Our key contributions can be summarized as follows.

- **Weak Supervision and Data-Free Operator Training:** We introduce a learning paradigm that requires no pre-computed solution data from expensive solvers like FEM. Our method bypasses the optimization challenges and computational costs of physics-informed losses by regressing against weak supervision from cheap and unbiased estimations of the stochastic PDE solvers, such as WoS [38]. We prove that such a paradigm shift from physics loss to stochastic loss reduces the GPU memory while achieving stronger generalization and efficiency.
- **Amortized Variance Reduction Across PDEs:** The proposed framework amortizes the cost of Monte Carlo walks across an entire distribution of PDE instances. Using weak supervision, the stochastic training process converges to the true solution operator, effectively learning to denoise the weak signals over the given family of Poisson PDEs.
- **Zero-Shot Generalization:** The trained operator can predict new PDE instances (e.g., with different boundary values, coefficient functions, or geometries) in a single forward pass, without retraining or additional simulations.

2. Background

We provide in this section the necessary background on WoS and neural operators to understand WoS-NO.

2.1. Monte Carlo Methods for PDEs

Grid-free Monte Carlo methods are particularly advantageous for problems involving complex geometries, high-dimensional spaces, or irregular domains where traditional grid-based numerical methods face significant meshing bottlenecks [39; 40; 46; 48]. The foundation of WoS [30] lies in the probabilistic interpretation of PDEs, specifically connecting the solution of Poisson equations to the expected values of stochastic Brownian motion. Crucially, WoS computes the solution at any query point independently, relying solely on the statistical properties of random walks without requiring a global mesh or linear system solve. While WoS has been successfully applied in computer graphics [38] and electrostatics [5], it relies on sampling efficiency. Recent approaches have introduced variance reduction techniques, such as gradient control variates [23; 38] and boundary value caching [28], to improve convergence rates. In the context of deep learning, hybrid approaches use neural networks for variance reduction [31] or as cached surrogates [21]. However, these methods largely focus on accelerating the WoS solver instead of using WoS as weak supervision for training.

2.2. Neural Operators

Neural operators define a class of discretization-agnostic, data-driven solvers that learn mappings between infinite-dimensional function spaces [3; 16; 26; 43]. Unlike traditional solvers that depend on fixed mesh resolutions, these methods learn integral kernel operators, allowing for zero-shot super-resolution. Despite their inference efficiency, standard neural operators are fundamentally data-driven. To reduce data dependence, Physics-Informed Neural Operators (PINO) integrate PDE constraints directly into the loss function [24]. However, PINO reintroduces significant optimization challenges: the loss landscape becomes highly complex, leading to training instabilities and sensitivity to hyperparameter tuning [25; 44]. Furthermore, PINO relies on automatic differentiation to compute PDE residuals, incurring high memory costs and scaling poorly with geometric complexity [31]. While recent approaches like the Multi-

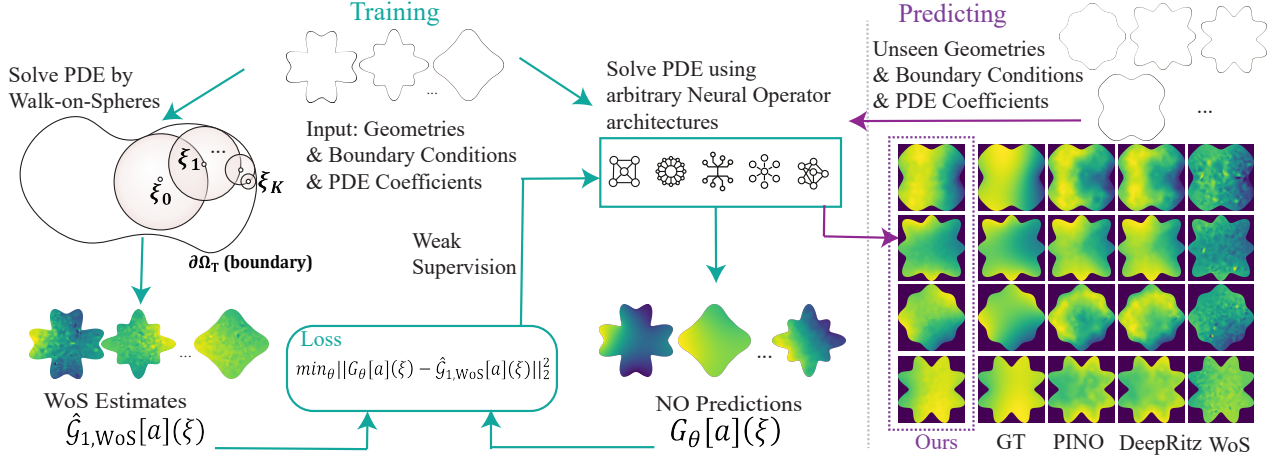


Figure 2. Weak Supervision Loss with WoS: Our algorithm learns the given family of parameterized Poisson equations $\Delta u = f$ on $\Omega_T \subset \mathbb{R}^d$ and $u|_{\partial\Omega_T} = g$ and is agnostic to underlying neural operator architecture. The WoS method defines the recursive process of the random walk, stopping once the boundary or the maximum number of steps is reached. The source contribution $f(\xi_i)$ is computed for each intermediate point ξ_i before jumping to the next point ξ_{i+1} . We achieve variance reduction by controlling the number of walks L to improve the fidelity of the weak solution. $\hat{\mathcal{G}}_{1,\text{WoS}}[a](\xi)$ denotes the estimation of 1-trajectory WoS estimation. ξ_K denotes the termination condition where the boundary value $g(\xi_K)$ is added if the point is within the tolerance region. The operator estimate is denoted by $\mathcal{G}_\theta[a](\xi)$. We illustrate the overall learning process, with WoS integral serving as the weak supervision for the neural operator.

Level Monte Carlo Operator (MLMC) attempt to accelerate training by decomposing the loss across fidelity levels [34], they still fundamentally rely on pre-computed ground truths. This creates a clear need for a training paradigm that is both data-free (like PINO) and computationally stable, a gap our WoS-NO framework addresses.

3. Problem Setting

Let $\Omega_T \subset \mathbb{R}^d$ be an open, bounded, connected, and sufficiently regular domain with $T \in \mathcal{T}$ as our distance function (e.g. signed distance function) defining the geometry. We consider the Poisson family of equations with source function family $f \in \mathcal{F}$, boundary function family $g \in \mathcal{B}$, and solution function family $u \in \mathcal{U}$. The parameterized elliptic PDE problem with Dirichlet boundary conditions is:

$$\begin{cases} \mathcal{P}[u] = f, & \text{on } \Omega_T, \\ u = g, & \text{on } \partial\Omega_T, \end{cases} \quad (1)$$

with a differential operator $\mathcal{P}[u] := \frac{1}{2}\text{Tr}(\sigma\sigma^\top \text{Hess}_u) + \mu \cdot \nabla u$. μ and σ represent the drift and diffusion terms.

Assuming the solution operator of the elliptic equation exists in the parameterized PDE family, our goal is to learn a solution operator $\mathcal{G} : \mathcal{A} = \mathcal{T} \times \mathcal{F} \times \mathcal{B} \rightarrow \mathcal{U}$, such that $a = (T, f, g) \mapsto u$, where u is the solution of the equation 1 over arbitrary combinations of T , f and g .¹

¹Whenever the context is clear, we write $\Omega_T \triangleq \Omega$ for simplicity

3.1. Walk-on-Spheres from the Operator Perspective

We generalize the derivation from neural Walk-on-Spheres [31] from the operator perspective. We first consider Poisson equations, which can be reformulated as stochastic differential equations driven by a random variable ξ , defined over the domain Ω_T . The stochastic differential equation is given by $dX_t^\xi = \mu(X_t^\xi)dt + \sigma(X_t^\xi)dW_t$, $X_0^\xi \sim \xi$, where W_t is a standard d -dimensional Wiener process, and μ and σ are time-dependent parameters with $\mu = 0$ and $\sigma = \sqrt{2}\mathbf{I}$ for Poisson equations.

By utilizing WoS, we can reformulate the solution operator $\mathcal{G}_{\text{WoS}} : \mathcal{A} \rightarrow \mathcal{U}$ for the Poisson equation as the expectation:

$$\mathcal{G}[a](\xi) = \mathcal{G}_{\text{WoS}}[a](\xi) = \mathbb{E}[g(X_{\tau}^\xi) - \sum_{k \geq 0} \int_0^{\tau_k} f(X_t^\xi) dt | \xi], \quad (2)$$

where we define $\tau_k = \tau(B_{r_k}, \xi_k) \triangleq \inf \{t \in [0, \infty) : X_t^{\xi_k} \notin B_{r_k}\}$ to be the stopping time within a sphere B of radius r_k centered at ξ_k and $r_k = \text{dist}(\xi_k, \partial\Omega_T) \in (0, \infty)$ at the k -th step of the random walk, $\tau = \tau(\Omega, \xi)$, and $\xi_{k+1} \sim X_{\tau_k}^{\xi_k} \sim \mathcal{U}(\partial B_{r_k}(\xi_k))$, $\xi_0 = \xi$. We defined more detailed derivations of each term in Appendix B.

In practice, we approximate the operator by $\mathcal{G}_{\text{WoS}}[a](\xi) \approx \hat{\mathcal{G}}_{L,\text{WoS}} = \frac{1}{L} \sum_{i=1}^L \text{WoS}^i[a](\xi)$, where L is the number of trajectories such that

$$\text{WoS}^i[a](\xi) = g(\xi_K^i) - \sum_{k=0}^{K-1} |B_{r_k^i}(\xi_k^i)| f(\gamma_k^i) G_{r_k^i}(\gamma_k^i, \xi_k^i), \quad (3)$$

where K is the maximum step, $a = (T, f, g) \in \mathcal{A}$, G is the Green's function (Appendix B), and $\gamma_k^i \sim \mathcal{U}(B_{r_k^i}(\xi_k^i))$.

Under the assumption that the solution exists as shown in [19], we have the equation $\mathcal{G}[a](\xi) = \mathcal{G}_{\text{WoS}}[a](\xi) \approx \hat{\mathcal{G}}_{L, \text{WoS}}[a](\xi)$, meaning that we can approximate the ground truth solution \mathcal{G} with stochastic estimator $\hat{\mathcal{G}}_{L, \text{WoS}}$ while controlling the fidelity with the number of trajectories L .

3.2. Walk-on-Spheres as Weak Supervision

We propose the following general loss form for families of parameterized Poisson equations as a cond. expectation

$$\mathcal{L}_\theta = \mathbb{E}[\|\mathcal{G}_\theta - \mathcal{G}\|^2] = \mathbb{E}[\mathbb{E}[\|\mathcal{G}_\theta[a](\xi) - \mathcal{G}_{\text{WoS}}[a](\xi)\|^2 | \xi]], \quad (4)$$

which follows from the tower property and the definition of the WoS operator.

Following [38], we generate *unbiased high-variance* weak supervision with WoS over a small number of trajectories $L \leq 10$. This allows fast ground truth generation on the fly in each epoch for regressing the neural operator. In practice however, we leverage early termination and caching over walks to accelerate WoS solver. This adds a non-zero bias to the estimate. The empirical loss then becomes

$$\hat{\mathcal{L}}_\theta = \frac{1}{NM} \sum_{j=1}^M \sum_{i=1}^N \|\mathcal{G}_\theta[a^j](\xi^i) - \hat{\mathcal{G}}_{L, \text{WoS}}[a^j](\xi^i)\|^2. \quad (5)$$

The entire pipeline is shown in more visual details in Figure 2. We add ablation studies on design choices and hyper-parameters in Appendix F.

4. Scene Setup

This section outlines the setups for our experiments. We structure our evaluation across two fundamental problem classes: linear Poisson with constant and varying coefficients. The WoS framework is most directly suitable for linear and screened forms of Poisson PDEs. In order to extend WoS to varying coefficients test cases, we linearized the governing equation into a screened form using the delta-tracking method [39] and formulated the delta-tracking variant of WoS loss for the operator. Our operator thereby takes both spatial coefficient functions and geometry as inputs.

4.1. Poisson Equations on parameterized domains

We follow the settings proposed in [32] to define a linear version of the Poisson equation on parameterized geometries as follows

$$\begin{aligned} \Delta u(x) &= f(x), & x \in \Omega_T \\ u(x) &= g(x), & x \in \partial\Omega_T \end{aligned} \quad (6)$$

where $u \in \mathcal{U}$ and $\Omega_T \subset \mathbb{R}^2$. The source function is a sum of radial basis functions denoted by $f(x) = \sum_{i=1}^2 \beta_i e^{\|x - \mu_i\|_2^2}$, where $\beta \in \mathbb{R}^1$ and $\mu_i \in \mathbb{R}^2$. The boundary term is a

periodic function defined in the polar-coordinate system as follows $g(x) = b_0 + b_1 \cos(\theta) + b_2 \sin(\theta) + b_3 \cos(2\theta) + b_4 \sin(2\theta)$, where $b_{0:4} \sim \mathcal{U}(-1, 1)$.

4.2. Second Order PDEs with spatially varying coefficients

We consider PDEs with spatially varying coefficients defined over irregular domains. The second-order elliptic PDE is denoted as

$$\begin{aligned} \nabla \cdot (\alpha \nabla u(x)) + \mathbf{v}\omega \cdot \nabla u(x) - \sigma u(x) &= -f(x) & x \in \Omega_T \\ u(x) &= g(x) & x \in \partial\Omega_T \end{aligned} \quad (7)$$

where, $\Omega_T \subset \mathbb{R}^3$ is the domain defined by distance T , $\alpha \in C^2(\Omega_T, \mathbb{R}_+)$, $\mathbf{v}\omega \in C^2(\Omega_T, \mathbb{R}^3)$, and $\sigma \in C(\Omega_T, \mathbb{R}_{>0})$. As presented in [21; 39], α is the *diffusion coefficient*, $\mathbf{v}\omega$ is the *drift coefficient* and σ denotes the *absorption coefficient*.

We consider a variant of this PDE by assuming $\mathbf{v}\omega = 0$, and define a delta-tracking-based WoS loss. This is done so by making the following substitutions to equation 7. $U(x) =$

$\sqrt{\alpha(x)}u(x)$, $g'(x) = \sqrt{\alpha(x)}g(x)$, $f'(x) = \frac{\sqrt{\alpha(x)}}{\alpha(x)}f(x)$, $\sigma'(x) = \frac{\sigma(x)}{\alpha(x)} + \frac{1}{2}(\frac{\Delta\alpha(x)}{\alpha(x)} + \frac{|\nabla \ln(\alpha(x))|^2}{2})$. This reformulation leads to a screened variant of equation 2:

$$\begin{aligned} \mathcal{G}_{\text{WoS}, \Delta}[a](\xi) &= \mathbb{E}[e^{-\bar{\sigma}\tau_k} g'(X_{\tau_k}^\xi) \\ &+ \sum_{k \geq 0} \int_0^{\tau_k} f(X_t^\xi, U) dt | \xi] \end{aligned} \quad (8)$$

As we can see from the above equation, the expectation depends on U , which is solved using the recursive delta-tracking algorithm, which we derive in Section C. This is adapted to a new loss function as follows:

$$\begin{aligned} \hat{\mathcal{L}}_{\theta, \Delta} &= \frac{1}{NM} \sum_{j=1}^M \sum_{i=1}^N \|\mathcal{G}_\theta[a^j, \alpha^i, \sigma^i](\xi^i) \\ &- \hat{\mathcal{G}}_{L, \text{WoS}, \Delta}[a^j](\xi^i)\|^2, \end{aligned} \quad (9)$$

where $\hat{\mathcal{G}}_{L, \text{WoS}, \Delta}[a^j](\xi^i)$ is an L-trajectory empirical mean of estimations with Delta tracking such that $\hat{\mathcal{G}}_{L, \text{WoS}, \Delta}[a](\xi) \approx \mathcal{G}_{\text{WoS}, \Delta}[a](\xi)$.

We provide an abstract view of the training pipeline of WoS-NO in Algorithm 1 and the definition of diffusion and absorption terms in Appendix C.

5. Experiments

This section presents the empirical validation of our proposed framework. The WoS framework is implemented using the *zombie C++* library [38]. We leverage python bindings to make calls from the training framework. While

we do not generate datasets for training, we generate domains (shapes) and PDE family coefficients. We provide the data generation and training details in Section D.

Our evaluation is structured into three parts: benchmarking against baseline methods, quantifying amortization gains, and demonstrating generalization to diverse applications.

First, we benchmark our framework against two classes of data-free PDE solvers: Physics-Informed Neural Operators (PINO) and Deep Ritz methods (which we extend from Yu et al. [47] to screened Poisson equations). For the comparison against the traditional Walk-on-Spheres solver, we conduct an equal sample analysis and equal time analysis. This involves averaging the outputs from multiple independent runs of both our trained operator and the WoS solver to evaluate and compare the consistency of their solutions under an identical sampling budget.

Second, we quantify the amortization gains of our operator, which is the computational speedup at inference time that offsets the initial cost of training. We measure this in two settings. For unseen PDE parameterizations, we quantify the gain by measuring the throughput of the traditional WoS solver; specifically, we calculate the number of new problem instances it can solve from scratch within the total wall-clock time required for our operator to converge to an L_2 relative error of 10^{-3} . To analyze scalability, we then compare the wall-clock time of our neural solver against the WoS solver across various resolutions, demonstrating our method’s efficiency on finer discretizations.

Finally, we showcase the versatility of our framework by applying it to a diverse set of domains beyond physics, including fluid dynamics and image inpainting. We include three key ablations in Section F - the effect of control-variates, the computational bottlenecks of online walks during training and lastly, the impact of number of walks L on performance.

5.1. Comparisons with Baselines

We benchmark our proposed WoS-NO against two established data-free baselines: the Physics-Informed Neural Operator (PINO) and the Deep Ritz Operator. We evaluate all methods on key metrics including training time, final accuracy on unseen PDEs, and computational resource consumption. The results are summarized in Table 1 and Table 2. Importantly, we focus on geometry aware multi-instance PDE solvers as our baselines to ensure fair comparison. As such we do not consider single instance geometry sensitive solvers such as neural walk on spheres (NWoS) [31] and neural cache solver [21]. Our work can be seen as an extension of these two architectures for the operator setting.

The data in Table 1 and Table 2 highlight the advantages of our method. Our WoS-NO achieves the lowest L_2 error while simultaneously reducing peak GPU memory and power consumption compared to both baselines. It remains faster than both PINO and Deepritz.

Table 1. Performance and compute comparison of our WoS-NO against data-free baselines on the linear Poisson family. All methods were trained for 20,000 steps, with the evaluation metrics averaged over 1000 unseen linear parameterizations. Our approach achieves the highest accuracy with significantly lower GPU resource consumption.

APPROACH	TRAINING TIME (Min)	AVERAGE MSE ERROR \pm Std	PEAK GPU MEMORY (MB)	PEAK GPU POWER (W)
PINO	85.25	$2.5e^{-3} \pm 4.7e^{-3}$	1523.5	78.43
Deepritz Operator	35.401	$1.0e^{-2} \pm 1.6e^{-2}$	859.43	49.52
WoS-NO	13.5	$8.2e^{-4} \pm 5.4e^{-4}$	627	48.81

Table 2. Performance and compute comparison of our WoS-NO against data-free baselines on Poisson equations with spatially varying coefficients. All methods were trained for 50,000 steps, with the evaluation metrics averaged over 1000 unseen spatially varying parameterizations. Our approach achieves the highest accuracy with significantly lower GPU resource consumption.

APPROACH	TRAINING TIME (Min)	AVERAGE MSE ERROR \pm Std	PEAK GPU MEMORY (MB)	PEAK GPU POWER (W)
PINO	411	$9.4e^{-3} \pm 1.1e^{-2}$	8587.9	122.85
Deepritz Operator	198	$1.1e^{-2} \pm 2.4e^{-2}$	3903.1	116.59
WoS-NO	188	$9.0e^{-3} \pm 7.9e^{-3}$	2886.3	103.90

In Figure 2 right, we make comparisons of predictions for the Poisson family over diverse geometries using WoS-NO, ground truth, PINO, DeepRitz, and WoS. We see that WoS-NO’s predictions are much closer to the ground truth than other methods. Moreover, while WoS results in very noisy predictions, WoS-NO smooths out noises from training and makes smooth predictions in different geometries, proving its efficiency and strong performance in learning the solution operator for parametrized PDEs with weak supervision.

5.2. Amortization

In order to make a fair comparison of performances between DeepRitz, PINO, and WoS-NO, we perform an equal time training comparison of the three methods with Poisson equations with spatially varying coefficients. We fix the number of training time to 200 minutes and train three models with optimized hyperparameters. Figure 3 left shows that under the fixed time framework, WoS-NO achieves the lowest L_2 -error ($9.0e^{-3}$) while converging fastest in comparison with both DeepRitz and PINO. Furthermore, we discover that PINO takes the longest to converge due to the computation of higher-order derivatives and its complex loss landscapes.

Furthermore, we compare for Poisson equations with spatially varying coefficients the amount of time it requires to achieve the same accuracy as a well-trained WoS-NO. As shown in Figure 3 middle, WoS requires roughly $7.2\times$ and $1.9\times$ longer inference time in comparison with WoS-NO to achieve the same level of L_2 error.

We further demonstrate the comparison of three architectures in inference on ShapeNet. Figure 1 shows that over 3 different geometries from ShapeNet, WoS-NO achieves the strongest zero-shot inference with $2.1\times$ overall improvement than PINO and $1.59\times$ than DeepRitz. Moreover, under the same time constraint, WoS-NO achieves $3.73\times$ better

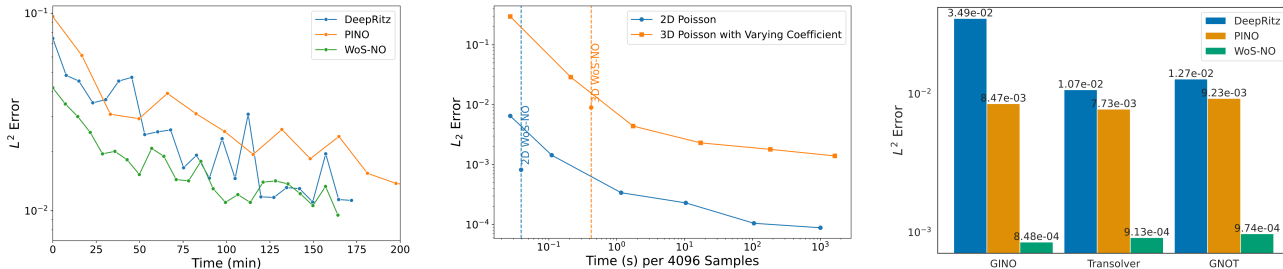


Figure 3. **Left:** Training Poisson equations with spatially varying coefficients with equal time for 200 minutes, WoS-NO demonstrates the lowest L_2 error while converging the fastest. In contrast, PINO requires a much longer time to converge. **Middle:** After WoS-NO training is finished, we compare the amount of time needed to achieve the same level of accuracy as L_2 -error to achieve the same L_2 error as a well-trained WoS-NO for 4096 pointwise estimations. **Right:** GINO, Transolver and GNOT are trained on DeepRitz, PINO and WoS-NO losses, and across all three operator architectures, WoS-NO is the strongest with the lowest L_2 -error.

performance than WoS, showing empirically that neural operators smooth out noises in stochastic estimations.

5.3. Architecture-Agnostic Loss

To demonstrate that WoS-NO is architecture-agnostic, we train GINO, Transolver and GNOT on linear Poisson equations with DeepRitz, PINO, and WoS-NO losses. As shown in Figure 3 right, regardless of which neural operator architecture we use, we see the lowest L_2 error with WoS-NO error in comparison with DeepRitz(100 \times) and PINO(10 \times). This shows that WoS-NO is a general framework that is applicable to any operator.

5.4. Generalization to Physical and Geometric Domains

A key advantage of our framework is its capacity for zero-shot generalization. To demonstrate this, we apply our operator, pre-trained on parametrized Poisson problems, to solve tasks from typical 2D and 3D problems that leverage Poisson methods, without any retraining or fine-tuning. This is made possible by reformulating each target problem with stochastic integrals. We discuss three classes of problems - von Karman vortex problem, biharmonic inpainting, and extending to Poisson surface reconstruction.

Biharmonic inpainting: We demonstrate the zero-shot generalization of our operator to higher-order PDEs by applying it to biharmonic image inpainting. The task is governed by the fourth-order equation $\Delta^2 u = 0$ within the masked image domain D . We reformulate this problem by introducing an intermediate function $v = \Delta u$, which decomposes the single fourth-order PDE into a system of two coupled second-order equations:

$$\begin{cases} \Delta v = 0, & \text{with } v|_{\partial D} = f \\ \Delta u = v, & \text{with } u|_{\partial D} = g \end{cases} \quad (10)$$

This system is solved recursively: we first apply our pre-trained operator to solve the Laplace equation for v , then use the resulting solution v as a source term to solve the Poisson equation for the final intensity u . For our evaluation, we in-

paint 20 masks, of dimensions 150x150 in pixel-space, and report the average performance. As shown in Figure 5, our method achieves competitive accuracy while being orders of magnitude faster than the traditional WoS solver. First, we apply our trained operator to solve the Laplace equation for v . Then, using the resulting solution v as a source term, we apply our operator a second time to solve the Poisson equation for the final image intensity u . For this problem, we consider a mask size of 150x150 pixels, and generate 20 masks, our results are the average over those. We present the results in Figure 5.

von Kármán Vortex: We investigate our operator’s utility as a fast, approximate solver by applying it to the pressure projection step of a von Kármán vortex simulation. This presents a particularly challenging zero-shot generalization task, as the simulation requires solving a sequence of previously unseen, screened Poisson equations with Neumann boundary conditions, a different problem class from our training data.

As shown in Figure 6, our operator offers a significant computational speedup compared to the traditional WoS solver. The resulting pressure field, while having an L_2 -relative error of $2.5e^{-1}$, is obtained orders of magnitude faster. This outcome highlights the operator as a fast, generalizable approximator but struggles with untrained boundary conditions. Its ability to produce an approximation at high speed paves the way for integrating it within hybrid methods, such as providing an early termination criterion for expensive Monte Carlo walks as proposed by [31], in the algorithms that incorporate Neumann conditions, such as Walk-on-Stars [40].

5.5. Comparison with FEM Solvers

To make further comparisons, we compare WoS-NO with FEM-based traditional solvers in terms of speed. As shown in Figure 4 left, we see that the FEM solver requires exponentially increasing inference time for inference in finer resolution. In contrast, while WoS cost increases slowly, WoS-NO has almost zero increase in time cost, demonstrating its scalability to high-fidelity PDEs.

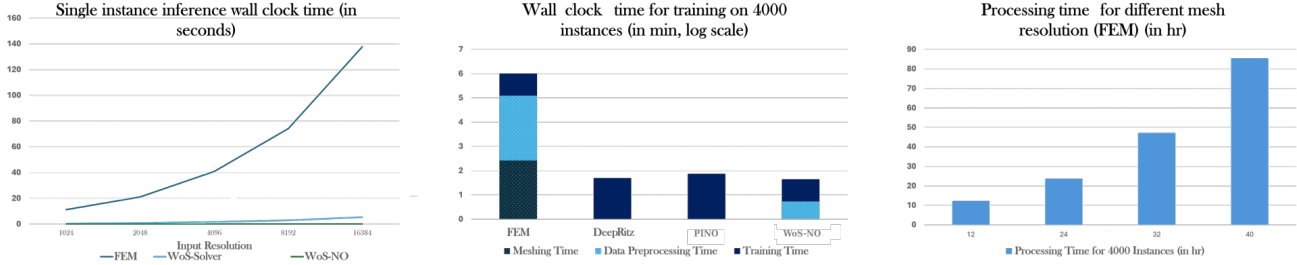


Figure 4. **Left:** This graph showcases the inference time of a single instance, as a function of domain size. In the case of FEM, it denotes the resolution of the mesh, while for the WoS-based methods, it’s the number of query points. **Middle:** This figure highlights the amortization achieved with our approach. Meshing time includes time needed to create meshes in the domain. Data preprocessing time includes the simulation time to create the regression target (FEM solution and WoS simulation). Training time represents the time required for the neural operator to learn the data-driven objective from the points sampled from the FEM solution. Our approach does not require meshing, and the total time for WoS-NO is lower than PINO while approximately equal to DeepRitz total time, making it an efficient operator for training. **Right:** This figure highlights how the data preprocessing time for FEM scales with the resolution of the inputs. Increasing the resolution results in a direct increase in computation time (hours). This is avoided by WoS-NO since WoS is highly parallelizable on GPU and does not depend on the input resolution.

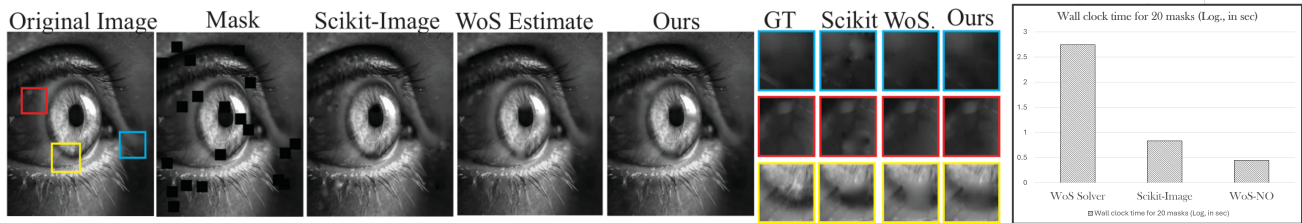


Figure 5. Quantitative comparison for biharmonic inpainting. We evaluate our pre-trained operator against a traditional WoS solver and the `scikit-image` baseline. The plot shows the final error versus total runtime (log scale, in seconds) required to inpaint 20 masks. The average MSE compared to the ground truth for our method is $2.8e^{-3} \pm 7.2e^{-3}$, WoS ($5.7e^{-3} \pm 5.2e^{-3}$) and `scikit-image` ($5.4e^{-3} \pm 5.0e^{-3}$). The total wall clock time for WoS solver is 557.2s, Scikit-Image 6.8s and WoS-NO 2.8s.

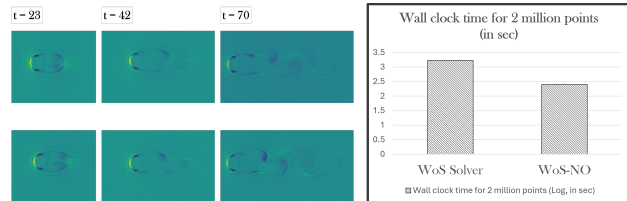


Figure 6. Qualitative and quantitative results showing the pressure field magnitude in the von Kármán vortex. **(Left)** Visual comparison of the pressure fields computed by the baseline WoS solver [12] (top) and our pre-trained operator (bottom). Our method achieves a relative error of 2.5×10^{-1} with respect to the baseline. **(Right)** Log-scale plot of the total wall-clock time required to compute the pressure solution over 70 simulation time-steps, comparing the computational cost of both methods. The total wall clock time for WoS solver is 1698.2s and WoS-NO 251.1s

In Figure 4 middle, we compare total training time, which includes data preprocessing time, meshing, and training time for FEM, DeepRitz, PINO and WoS-NO. FEM demonstrates the highest total time due to its requirement for meshing and processing for solutions. While WoS-NO requires extra time for preprocessing to perform random walks, the total training time is much smaller than other methods since it avoids computations of gradients over higher-order derivatives.

Figure 4 right demonstrates the processing time for FEM

with an increase in mesh resolution. We see that as we increase the mesh resolution from 12 to 40 ($4\times$), the data preprocessing time increases $8\times$, making it not scalable to higher and finer resolution tasks. In contrast, WoS-NO’s processing time uses random walks with WoS and is highly parallelizable with GPU. Moreover, it is a meshless method and is independent of the resolution grid. As a result, it is a much more scalable option for complex geometries with fine resolutions.

6. Future Work

A challenging test for the generalizability of a PDE solver is Poisson surface reconstruction. Current methods, such as physics-informed neural fields, often require per-scene optimization and struggle to generalize to new inputs without retraining. Our framework, however, can be applied in a zero-shot manner by reformulating the task as a Poisson problem. The standard approach seeks to find an indicator function χ of the surface’s interior whose Laplacian equals the divergence of the input point cloud’s normal field, N , i.e., $\Delta\chi = \nabla \cdot N$. One promising direction is to model the surface reconstruction as a stochastic integral; such an approach, which we leave for future work, could pave the way for a *truly general-purpose, training-data-free foundational Poisson solver*.

Impact Statement

This paper presents work whose goal is to advance the field of Machine Learning. There are many potential societal consequences of our work, none which we feel must be specifically highlighted here.

Acknowledgment

A. Anandkumar and X. Deng are both supported in part by the Bren endowed chair and the AI2050 senior fellow program at Schmidt Sciences.

References

- [1] Aksyuk, I. A., Kireeva, A. E., Sabelfeld, K. K., and Smirnov, D. D. Stochastic simulation algorithms for iterative solution of the lamé equation. *Numerical Analysis and Applications*, 16(4):299–316, 2023.
- [2] Alkin, B., Fürst, A., Schmid, S., Gruber, L., Holzleitner, M., and Brandstetter, J. Universal physics transformers. *CoRR*, 2024.
- [3] Azizzadenesheli, K., Kovachki, N., Li, Z., Liu-Schiaffini, M., Kossaifi, J., and Anandkumar, A. Neural operators for accelerating scientific simulations and design. *Nature Reviews Physics*, pp. 1–9, 2024.
- [4] Baldi, P. *Stochastic Calculus: An Introduction Through Theory and Exercises*. Universitext. Springer International Publishing, 2017.
- [5] Bossy, M., Champagnat, N., Maire, S., and Talay, D. Probabilistic interpretation and random walk on spheres algorithms for the poisson-boltzmann equation in molecular dynamics. *ESAIM: Mathematical Modelling and Numerical Analysis*, 44(5):997–1048, 2010.
- [6] Chang, A. X., Funkhouser, T., Guibas, L., Hanrahan, P., Huang, Q., Li, Z., Savarese, S., Savva, M., Song, S., Su, H., et al. Shapenet: An information-rich 3d model repository. *arXiv preprint arXiv:1512.03012*, 2015.
- [7] Chong, C., Kumar, A. S., and Lee, H. Automatic mesh-healing technique for model repair and finite element model generation. *Finite Elements in Analysis and Design*, 43(15):1109–1119, 2007.
- [8] Dodik, A., Sitzmann, V., Solomon, J., and Stein, O. Robust biharmonic skinning using geometric fields. *ACM Transactions on Graphics*, 2024.
- [9] Hao, Z., Wang, Z., Su, H., Ying, C., Dong, Y., Liu, S., Cheng, Z., Song, J., and Zhu, J. Gnot: A general neural operator transformer for operator learning. In *International Conference on Machine Learning*, pp. 12556–12569. PMLR, 2023.
- [10] Hwang, C.-O., Given, J. A., and Mascagni, M. On the rapid estimation of permeability for porous media using brownian motion paths. *Physics of Fluids*, 12(7):1699–1709, 2000.
- [11] Hwang, C.-O., Mascagni, M., and Won, T. Monte carlo methods for computing the capacitance of the unit cube. *Mathematics and Computers in Simulation*, 80(6):1089–1095, 2010.
- [12] Jain, P., Qu, Z., Chen, P. Y., and Stein, O. Neural monte carlo fluid simulation. In *ACM SIGGRAPH 2024 Conference Papers*, pp. 1–11, 2024.
- [13] Kablukova, E., Sabelfeld, K. K., Protasov, D., and Zhuravlev, K. Stochastic simulation of electron transport in a strong electrical field in low-dimensional heterostructures. *Monte Carlo Methods and Applications*, 29(4):307–322, 2023.
- [14] Kim, J.-H. and Lee, J. Learning representation of turbulent vector fields via efficient moving least squares based on monte carlo method. *IEEE Access*, 2025.
- [15] Kotsinis, D., Karras, G. C., and Bechlioulis, C. P. Autonomous exploration in unknown indoor 2d environments using harmonic fields and monte carlo integration. *Sensors*, 25(16):4894, 2025.
- [16] Kovachki, N., Li, Z., Liu, B., Azizzadenesheli, K., Bhattacharya, K., Stuart, A., and Anandkumar, A. Neural operator: Learning maps between function spaces with applications to pdes. *Journal of Machine Learning Research*, 24(89):1–97, 2023.
- [17] Krishnapriyan, A., Gholami, A., Zhe, S., Kirby, R., and Mahoney, M. W. Characterizing possible failure modes in physics-informed neural networks. *Advances in neural information processing systems*, 34:26548–26560, 2021.
- [18] Le Coz, Y. and Iverson, R. A stochastic algorithm for high speed capacitance extraction in integrated circuits. *Solid-State Electronics*, 35(7):1005–1012, 1992.
- [19] Le Gall, J.-F. *Brownian motion, martingales, and stochastic calculus*. Springer, 2016.
- [20] Li, X., Li, Z., Kovachki, N., and Anandkumar, A. Geometric operator learning with optimal transport. *arXiv preprint arXiv:2507.20065*, 2025.
- [21] Li, Z., Yang, G., Deng, X., De Sa, C., Hariharan, B., and Marschner, S. Neural caches for monte carlo partial differential equation solvers. In *SIGGRAPH Asia 2023 Conference Papers*, pp. 1–10, 2023.
- [22] Li, Z., Kovachki, N., Choy, C., Li, B., Kossaifi, J., Otta, S., Nabian, M. A., Stadler, M., Hundt, C., Azizzadenesheli, K., et al. Geometry-informed neural operator for large-scale 3d pdes. *Advances in Neural Information Processing Systems*, 36, 2024.

- [23] Li, Z., Yang, G., Zhao, Q., Deng, X., Guibas, L., Hariharan, B., and Wetzstein, G. Neural control variates with automatic integration. In *ACM SIGGRAPH 2024 Conference Papers*, pp. 1–9, 2024.
- [24] Li, Z., Zheng, H., Kovachki, N., Jin, D., Chen, H., Liu, B., Azizzadenesheli, K., and Anandkumar, A. Physics-informed neural operator for learning partial differential equations. *ACM/JMS Journal of Data Science*, 1(3):1–27, 2024.
- [25] Lin, R. Y., Berner, J., Duruisseaux, V., Pitt, D., Leibovici, D., Kossaifi, J., Azizzadenesheli, K., and Anandkumar, A. Enabling automatic differentiation with mollified graph neural operators. *arXiv preprint arXiv:2504.08277*, 2025.
- [26] Lu, L., Jin, P., Pang, G., Zhang, Z., and Karniadakis, G. E. Learning nonlinear operators via deepoNet based on the universal approximation theorem of operators. *Nature machine intelligence*, 3(3):218–229, 2021.
- [27] Mascagni, M. and Simonov, N. A. Monte carlo methods for calculating some physical properties of large molecules. *SIAM journal on scientific computing*, 26(1):339–357, 2004.
- [28] Miller, B., Sawhney, R., Crane, K., and Gkioulekas, I. Boundary value caching for walk on spheres. *arXiv preprint arXiv:2302.11825*, 2023.
- [29] Miller, B., Sawhney, R., Crane, K., and Gkioulekas, I. Solving partial differential equations in participating media. *ACM Transactions on Graphics (TOG)*, 44(4):1–21, 2025.
- [30] Muller, M. E. Some continuous monte carlo methods for the dirichlet problem. *The Annals of Mathematical Statistics*, pp. 569–589, 1956.
- [31] Nam, H. C., Berner, J., and Anandkumar, A. Solving poisson equations using neural walk-on-spheres. *arXiv preprint arXiv:2406.03494*, 2024.
- [32] Qin, T., Beatson, A., Oktay, D., McGreivy, N., and Adams, R. P. Meta-pde: Learning to solve pdes quickly without a mesh. *arXiv preprint arXiv:2211.01604*, 2022.
- [33] Rodriguez, H. R., Huang, J., and Yu, W. Deepwcap: Neural-guided random-walk capacitance solver for ic design. *arXiv preprint arXiv:2511.06831*, 2025.
- [34] Rowbottom, J., Fresca, S., Lio, P., Schönlieb, C.-B., and Boullé, N. Multi-level monte carlo training of neural operators. *arXiv preprint arXiv:2505.12940*, 2025.
- [35] Sabelfeld, K. Correlation structure of the solution to the reaction-diffusion equation in respond to random fluctuations of the boundary conditions. *Fluctuation and Noise Letters*, 23(01):2450001, 2024.
- [36] Sabelfeld, K. K. and Bukhasheev, O. Global random walk on grid algorithm for solving navier–stokes and burgers equations. *Monte Carlo Methods and Applications*, 28(4):293–305, 2022.
- [37] Sanz-Alonso, D. and Al-Ghattas, O. A first course in monte carlo methods. *arXiv preprint arXiv:2405.16359*, 2024.
- [38] Sawhney, R. and Crane, K. Monte carlo geometry processing: A grid-free approach to pde-based methods on volumetric domains. *ACM Transactions on Graphics*, 39(4), 2020.
- [39] Sawhney, R., Seyb, D., Jarosz, W., and Crane, K. Grid-free monte carlo for pdes with spatially varying coefficients. *ACM Transactions on Graphics (TOG)*, 41(4):1–17, 2022.
- [40] Sawhney, R., Miller, B., Gkioulekas, I., and Crane, K. Walk on stars: A grid-free monte carlo method for pdes with neumann boundary conditions. *arXiv preprint arXiv:2302.11815*, 2023.
- [41] Shalimova, I. and Sabelfeld, K. Random walk on spheres method for solving anisotropic transient diffusion problems and flux calculations. *Monte Carlo Methods and Applications*, 30(1):73–80, 2024.
- [42] Tran, P. D., Blanpied, T. A., and Atzberger, P. J. Protein drift-diffusion dynamics and phase separation in curved cell membranes and dendritic spines: Hybrid discrete-continuum methods. *Physical Review E*, 106(4):044402, 2022.
- [43] Viswanath, H., Rahman, M. A., Vyas, A., Shor, A., Medeiros, B., Hernandez, S., Prameela, S. E., and Bera, A. Neural operator: Is data all you need to model the world? an insight into the impact of physics informed machine learning. *arXiv preprint arXiv:2301.13331*, 2023.
- [44] Wang, S., Teng, Y., and Perdikaris, P. Understanding and mitigating gradient flow pathologies in physics-informed neural networks. *SIAM Journal on Scientific Computing*, 43(5):A3055–A3081, 2021.
- [45] Wu, H., Luo, H., Wang, H., Wang, J., and Long, M. Transolver: A fast transformer solver for pdes on general geometries. *arXiv preprint arXiv:2402.02366*, 2024.
- [46] Yilmazer, E. F., Vicini, D., and Jakob, W. Solving inverse pde problems using grid-free monte carlo estimators. *ACM Transactions on Graphics (TOG)*, 43(6):1–18, 2024.
- [47] Yu, B. et al. The deep ritz method: a deep learning-based numerical algorithm for solving variational problems. *Communications in Mathematics and Statistics*, 6(1):1–12, 2018.

- [48] Yu, Z., Wu, L., Zhou, Z., and Zhao, S. A differential monte carlo solver for the poisson equation. In *ACM SIGGRAPH 2024 Conference Papers*, pp. 1–10, 2024.

A. Background: Operator Learning

A neural operator [16] is a data-driven approximation of mappings between function spaces denoted as $\mathcal{G}_\theta : \mathcal{A} \rightarrow \mathcal{U}$ such that $\mathcal{G}_\theta \approx \mathcal{G}$, where \mathcal{G} is defined in equation 3.

A neural operator is composed of pointwise and integral operators, which can be represented as the discretization of the kernel-integral transform, where the learnable kernel is parameterized by neural networks. In our work, we propose the use of neural operators to learn the integral presented in Equation (2). We define a neural operator based on GINO [22] to approximate the unknown Green's function by formulating it as a kernel integral as shown below

$$\mathcal{G}[a](\xi) = u(\xi; a) := \int_{\Omega_T} \kappa_\theta(\xi, \gamma) a(\gamma) d\gamma. \quad (11)$$

In the discrete setting, this is represented as a summation, denoted as

$$\mathcal{G}[a](\xi) \approx \sum_j \kappa_\theta(\xi, \gamma_j) a(\gamma_j). \quad (12)$$

We follow the model architecture presented in GINO [22]. The input, represented as point clouds, is projected onto a uniform latent grid, and the input functions $a = (f, g, T)$ are integrated by the FNO. We use a second GNO to evaluate the integral over a desired set of validation points defined over the same spatial domain but may differ from the input point clouds.

B. Derivation of Walk-on-Spheres

We present a more detailed derivation of Walk-on-Spheres.

Given equation 3.1, we apply Itô's lemma to the process $u(X_t^\xi)$ and can reformulate the Poisson equation as

$$g(X_\tau^\xi) = u(\xi) + \int_0^\tau f(X_t^\xi) dt + \sqrt{2} \int_0^\tau \nabla u(X_t^\xi) dW_t, \quad (13)$$

where $\tau = \tau(\Omega, \xi) = \inf\{t \in [0, \infty) : X_t^\xi \notin \Omega\}$ is the stopping time or the first exit time of the stochastic process from the domain Ω .

By writing the equation in an expectation form, we can get

$$u(x) = \mathbb{E} \left[g(X_\tau^\xi) - \int_0^\tau f(X_t^\xi) dt \mid \xi = x \right], \quad (14)$$

since $\int_0^\tau \nabla u(X_t^\xi) dW_t$ has an expectation zero, see, e.g., Baldi [4, Theorem 10.2].

By restricting the domain Ω to an open sub-domain $\Omega_0 \subset \Omega$ with $\xi_0 = \xi \in \Omega_0$ and $\tau_0 = \tau(\Omega_0, \xi)$, we can rewrite the expectation as

$$u(\xi) = \mathbb{E} \left[u(X_{\tau_0}^\xi) - \int_0^{\tau_0} f(X_t^{\xi_0}) dt \mid \xi \right]. \quad (15)$$

To recursively solve the equation, we further define the random variable $\xi_1 \sim X_{\tau_0}^\xi$ with sub-domain $\Omega_1 \subset \Omega$ containing ξ_1 and $\tau_1 = \tau(\Omega_1, \xi_1)$. We get

$$u(X_{\tau_0}^\xi) \sim u(\xi_1) = \mathbb{E} \left[u(X_{\tau_1}^{\xi_1}) - \int_0^{\tau_1} f(X_t^{\xi_1}) dt \mid \xi_1 \right]. \quad (16)$$

As a result, we can define a recursive solution

$$u(\xi) = \mathbb{E} \left[g(X_\tau^\xi) - \sum_{k \geq 0} \int_0^{\tau_k} f(X_t^{\xi_k}) dt \mid \xi \right]. \quad (17)$$

The second term in 17 can be computed by using Green's function such that

$$\mathbb{E}\left[\int_0^{\tau_k} f(X_t^\xi) dt\right] = \int_{B_{r_k}(\xi_k)} f(y) G(\xi_k, y) dy \quad (18)$$

which can be solved through Monte Carlo integrations such that

$$\mathbb{E}\left[\int_0^{\tau_k} f(X_t^\xi) dt\right] = |B_{r_k}(\xi_k)| \mathbb{E}[f(y) G_{r_k}(y, \xi_k)] \quad (19)$$

where $y \sim \mathcal{U}(B_{r_k}(\xi_k))$ and

$$G_r(y, z) := \begin{cases} \frac{1}{2\pi} \log \frac{r}{\|y-z\|}, & d = 2, \\ \frac{\Gamma(d/2-1)}{4\pi^{d/2}} (\|y-z\|^{2-d} - r^{2-d}), & d > 2, \end{cases} \quad (20)$$

C. Derivation of Delta Tracking

We follow the derivation presented in [39].

Let us define the PDE to be as follows

$$\begin{aligned} \nabla \cdot (\alpha(x) \nabla u) - \sigma u(x) &= -f(x), & x \in \Omega \\ u(x) &= g(x), & x \in \partial\Omega \end{aligned} \quad (21)$$

We expand the second order term and apply the identity $\nabla \ln(\alpha(x)) = \nabla \alpha(x) / \alpha(x)$

$$\Delta u(x) + \nabla \ln(\alpha(x)) \cdot \nabla u(x) - \frac{\sigma(x)}{\alpha(x)} u(x) = -\frac{f(x)}{\alpha(x)} \quad (22)$$

We eliminate the first order operator by applying Girsanov transformation.

$$\begin{aligned} \Delta U(x) - \sigma'(x) U(x) &= -f'(x), & x \in \Omega \\ U(x) &= g'(x), & x \in \partial\Omega \end{aligned} \quad (23)$$

Where, $U(x) = \sqrt{\alpha(x)} u(x)$, $g'(x) = \sqrt{\alpha(x)} g(x)$, $f'(x) = \frac{\sqrt{\alpha(x)}}{\alpha(x)} f(x)$, $\sigma'(x) = \frac{\sigma(x)}{\alpha(x)} + \frac{1}{2} \left(\frac{\Delta \alpha(x)}{\alpha(x)} + \frac{|\nabla \ln(\alpha(x))|^2}{2} \right)$

We introduce a coefficient $\bar{\sigma} > 0$, to shift the heterogeneity to a source term. The equation then becomes

$$\begin{aligned} \Delta U(x) - \bar{\sigma} U(x) &= -f'(x, U), & x \in \Omega \\ U(x) &= g'(x), & x \in \partial\Omega \end{aligned} \quad (24)$$

where $f'(x, U) = f'(x) + (\bar{\sigma} - \sigma'(x)) U(x)$. Using the Feynman-Kac formulation, we derive

$$U(\xi) = \mathbb{E}[e^{-\bar{\sigma}\tau} g'(X_\tau^\xi) + \int_0^\tau e^{-\bar{\sigma}t} f'(X_t^\xi, U) dt | \xi]. \quad (25)$$

Similar to the derivation of the original Walk-on-Spheres, we define the integral as

$$U(X_{\tau_0}^\xi) \sim u(\xi_1) = \mathbb{E}[e^{-\bar{\sigma}\tau_1} U(X_{\tau_1}^{\xi_1}) + \int_0^{\tau_1} e^{-\bar{\sigma}t} f'(X_t^{\xi_1}, U) dt | \xi_1]. \quad (26)$$

By solving this recursively, we find that

$$U(\xi) = \mathbb{E}[(\Pi_{k \geq 0} e^{-\bar{\sigma}\tau_k}) g'(X_\tau^\xi) + \sum_{k \geq 0} (\Pi_{i \leq k} e^{-\bar{\sigma}\tau_i}) \int_0^{\tau_k} e^{-\bar{\sigma}t} f'(X_t^{\xi_k}, U) dt | \xi]. \quad (27)$$

To evaluate the solution iteratively, we need to reformulate $\mathbb{E}[e^{-\bar{\sigma}\tau_k}U(X_{\tau_k}^{\xi_k})|\xi_k]$ and $\mathbb{E}[\int_0^{\tau_k} e^{-\bar{\sigma}t}U(X_t^{\xi_k})dt|\xi_k]$.

The first term can be approximated using the Poisson kernel $P^{\bar{\sigma}}$

$$\mathbb{E}[e^{-\bar{\sigma}\tau_k}U(X_{\tau_k}^{\xi_k})|\xi_k] = \int_{\partial B_{r_k}(\xi_k)} U(z)P^{\bar{\sigma}}(z)dz, \quad (28)$$

and the second term can be approximated using Green's function $G^{\bar{\sigma}}$

$$\mathbb{E}[\int_0^{\tau_k} e^{-\bar{\sigma}t}U(X_t^{\xi_k})dt|\xi_k] = \int_{B_{r_k}(\xi_k)} f'(y, U)G^{\bar{\sigma}}(\xi_k, y)dy, \quad (29)$$

As such, the new integral can be recursively represented as a solution operator \mathcal{G}_Δ of screened Poisson equations

$$\begin{aligned} \hat{\mathcal{G}}_\Delta[a](\xi) &= \frac{1}{\sqrt{\alpha(\xi)}} \left(\int_{B(c)} f(y)G^{\bar{\sigma}}(\xi, y)dy + \right. \\ &\quad \left. \int_{\partial B(c)} \sqrt{\alpha(z)}\hat{\mathcal{G}}_\Delta[a](z)P^{\bar{\sigma}}(\xi, z)dz \right) \end{aligned} \quad (30)$$

where, $G^{\bar{\sigma}}$ is Green's function and $P^{\bar{\sigma}}$ is the Poisson kernel, given by the normal derivative of Green's function at the boundary. Refer [39] for more detailed derivations.

C.1. Definition of terms for Poisson with spatially varying coefficients

In this section, we define all terms in spatially-varying coefficient Poisson as shown in Section 4

Boundary term g : We define the boundary term using the parametric equation $g(x) = \sin(\pi\Phi_\alpha x_0) \cos(2\pi\Phi_\alpha x_1) + (1 - \cos(\pi\Phi_\alpha x_0))(1 - \sin(2\pi\Phi_\alpha x_1)) + \sin^2(3\pi\Phi_\alpha x_2)$, where Φ_α is the diffusion frequency. We denote that $u(x) = g(x)$.

Diffusion Coefficient α : Diffusion coefficient describes the rate of diffusion of a physical quantity (e.g. heat) in a spatial medium. We define it as $\alpha(x) = \exp(-x_1^2 + \cos(4\pi\Phi_\alpha x_0) \sin(3\pi\Phi_\alpha x_1))$

Absorption Coefficient σ : Absorption coefficient allows for damping and amplification and is denoted as $\sigma(x) = A_{min} + (A_{max} - A_{min})(1 + 0.5 \sin(2\pi x_0) \cos(0.5\pi x_1))$, where A_{max} and A_{min} are coefficients representing the minimum and maximum values for absorption.

Source term f : We compute the source term as $f(x) = -\alpha\nabla^2 u - \nabla\alpha \cdot u + \sigma u$. We approximate the gradient and the Laplacian from the closed-form expression.

D. Experimental Settings

D.1. Domain Generation

Linear Setting For the linear settings, we generate the domain Ω_T by sampling points in the polar coordinate system. The domain Ω_T is disc-like, centered at the origin with its boundary radius defined by $r(\theta) = r_0[1 + c_1 \cos(4\theta) + c_2 \cos(8\theta)]$. We fix $r_0 = 1$, and c_1, c_2 are varying parameters uniformly sampled such that $c_1, c_2 \sim \mathcal{U}(-0.2, 0.2)$. To sample points inside the domain, we use a rejection-sampling strategy to ensure that all points lie strictly inside the boundary. For any candidate point (x_0, x_1) , we compute its polar coordinates, specifically the angle $\theta = \arctan2(x_1, x_0)$ and the radial distance $r = \sqrt{x_0^2 + x_1^2}$. A point is deemed to belong to the domain if $r < r_0$, where r_0 is calculated for the given θ . We first over-sample a uniform grid of candidate points in the rectangular region enclosing Ω . Each candidate point is evaluated against the domain boundary to determine whether it is within. Points that satisfy this criterion are retained, and the desired number of domain points is then sampled uniformly from the retained set. This approach ensures that the sampled points represent the geometry of the domain. In contrast, boundary points are explicitly generated by evaluating parametric boundary equations for uniformly spaced values of θ . This guarantees an accurate representation of the domain boundary for enforcing Dirichlet boundary conditions.

Varying Coefficient Setting For the experiments with Poisson with varying coefficients, we use meshes from the ShapeNet dataset [6] to define complex geometries. To sample domain and boundary points, we compute a fast signed distance field (SDF) estimate using the Bounding Volume Hierarchy (BVH). Domain points are identified by evaluating the SDF of a set of candidate points relative to the mesh, where points with a negative SDF (indicating that they lie inside the mesh) are retained. Boundary points are sampled by selecting points with an absolute SDF value within a small threshold $\epsilon = 0.01$, corresponding to points located at a distance of approximately ϵ from the mesh surface. The use of BVH speeds up the SDF computation by efficiently finding the nearest points on the mesh surface.

Algorithm 1 Training of WoS-NO

- 1: **Input:** Neural operator \mathcal{G}_θ parameterized by θ , epochs E , distance function T , source term f , bound term g , WoS operator $\hat{\mathcal{G}}_{L, \text{WoS}}$, trajectories L , domain Ω_T , input space $\mathcal{A} = \mathcal{T} \times \mathcal{F} \times \mathcal{B}$, learning rate γ
 - 2: **Output:** Learned parameters θ
 - 3: **for** $i = 0$ to E **do**
 - 4: $a = (T, f, g) \sim \mathcal{A}$
 - 5: $\{\xi^j\}_j \sim \Omega_T$
 - 6: $\{y^j\}_j \leftarrow \text{vmap}[\hat{\mathcal{G}}_{L, \text{WoS}}[a]](\{\xi^j\}_j)$
 - 7: $\hat{\mathcal{L}}(\theta) \leftarrow \text{MSE}(\mathcal{G}_\theta[a](\xi^j), y^j)$
 - 8: $\theta \leftarrow \text{step}(\gamma, \nabla_\theta \hat{\mathcal{L}}(\theta))$
 - 9: **end for**
-

E. Training details

We train our model on a set of 4000 PDE instances defined over unique geometries. As our framework is primarily architecture independent, we leverage 3 architectures within the neural operator class - GINO [22], GNOT [9] and Transolver [45]. During training, we sample 1024 domain and boundary points, respectively, from the instance and this forms the input to the model, alongside the pointwise source, (diffusion, and absorption for the varying coefficient case) values computed on the samples. We evaluate the performance on unseen geometries and unseen PDE parameters. To train the model, we use the Adam optimizer, with a learning rate of 1e-3 and a weight decay of 1e-6. We use the linear WoS-based residual for the linear and the delta tracking residual for the varying coefficient one. The training process includes a learning rate scheduler (*ReduceLRonPlateau*), which reduces the learning rate by a factor of 0.9 when the validation loss stagnates for 2 consecutive epochs. All experiments were performed on NVIDIA RTX 3060 GPU.

E.1. Caching prior walks

Inspired by [31], we use a cache to store intermediate walks $\{(a^j, \xi^i, \hat{\mathcal{G}}_{L, \text{WoS}}[a^j](\xi^i))\}_{i,j}$. Instead of relying on a fixed, noisy target, the cached estimate is updated each epoch with a small number of fresh Monte Carlo walks. This process amortizes the variance reduction over the training duration. The cache incurs an additional space complexity of $O(mn)$, where m is the number of instances in the training dataset and n is the number of points per instance.

Let k be the current training epoch and L be the number of new WoS trajectories generated per epoch for each point. The cached target estimate at epoch k , which we denote as $Y_{j,i}^{(k)}$, is the running average of all $k \cdot L$ trajectories generated up to that point. This can be expressed via the following recursive update rule:

$$Y_{j,i}^{(k)} = \frac{k-1}{k} Y_{j,i}^{(k-1)} + \frac{1}{k} \hat{\mathcal{G}}_{L, \text{WoS}}^{(k, \text{new})}[a^j](\xi^i) \quad \text{with} \quad Y_{j,i}^{(0)} = 0 \quad (31)$$

where $\hat{\mathcal{G}}_{L, \text{WoS}}^{(k, \text{new})}$ is the estimate derived from the L fresh walks generated during epoch k . As the training progresses ($k \rightarrow \infty$), the variance of our target approaches zero, and $Y_{j,i}^{(k)}$ converges to the true solution $\mathcal{G}[a^j](\xi^i)$. The empirical loss at epoch k is therefore a function of this refined target:

$$\hat{\mathcal{L}}_\theta^{(k)} = \frac{1}{NM} \sum_{j=1}^M \sum_{i=1}^N \|\mathcal{G}_\theta[a^j](\xi^i) - Y_{j,i}^{(k)}\|^2 \quad (32)$$

E.2. Hyperparameters for the models

GINO For the GINO module, an embedding dimension of 16, with a maximum of 600 positional embeddings. The graph construction radii for input, and output, were set to 0.1, 0.1, and 0.05, respectively. The input and output transforms are

linear; the input channel MLP has hidden layers of [4, 256, 512, 256, 3] and the output channel MLP has layers of [128, 512, 1024, 512, 64]. The FNO module consists of 4 layers with [20, 20] Fourier modes. The hidden, lifting, and projection channel dimensions were set to 64, 256, and 64, respectively. We used Group Normalization, a channel MLP expansion factor of 0.5, 8 features for AdaIn, and a tensor factorization rank of 0.8.

GNOT The GNOT model is a Transformer-based architecture with 12 layers with a hidden dimension of 128. The attention mechanism employs a single head with a linear attention type and no dropout. The feed-forward network is a Mixture-of-Experts model with 2 experts. Each expert’s MLP is composed of 2 layers with an inner dimension of 8, and no dropout is applied. Horizontal Fourier features were not used.

Transolver The Transolver model is a Transformer-based architecture configured with 6 layers, a hidden dimension of 32, and 24 attention heads. The model incorporates residual connections and is set with a slice number of 32 and a reference value of 16. It does not use time as an input feature and is designed to produce a single scalar output.

F. Ablations

In this section, we provide different ablation studies for improving the performance of WoS-NO.

F.1. Effects of Control Variates

As discussed in [38], control variates provide a principled approach to reducing the variance of Walk-on-Spheres estimates, leading to more consistent and accurate results. However, in our case, we observe no significant improvements, due to the expressivity of neural operators and their ability to learn from noisy inputs.

Table 3. Showcasing the effects of control variates on the 2D dataset.

CONTROL VARIATES	TRAIN L2 Err	TEST L2 Err
No	$4.05e^{-4}$	$8.2e^{-4}$
Yes	$4.33e^{-4}$	$8.35e^{-4}$

F.2. Effects of Number of Trajectories

To evaluate the impact of the number of trajectories for WoS-NO. We train WoS-NO with $L = 1, 10, 100, 1000$ to evaluate the influence of the number of trajectories for WoS-No.

As shown in Figure 7 left, the number of trajectories has a direct influence on the training time. The higher the number of trajectories, the lower the variance and the longer the simulation time for full convergence of random walks. This results in a trade-off between fidelity and simulation time and requires careful tuning to balance two costs. We further evaluated the validation loss for different numbers of trajectories in Figure 7 right. We discover that asymptotically, the performance of WoS-NO converges to a similar validation loss level, proving that neural operators are able to smooth out noises in stochastic estimations in the long term. We choose $L = 10$ as we find that it has slight improvements in the final performance while not introducing significant costs for training.

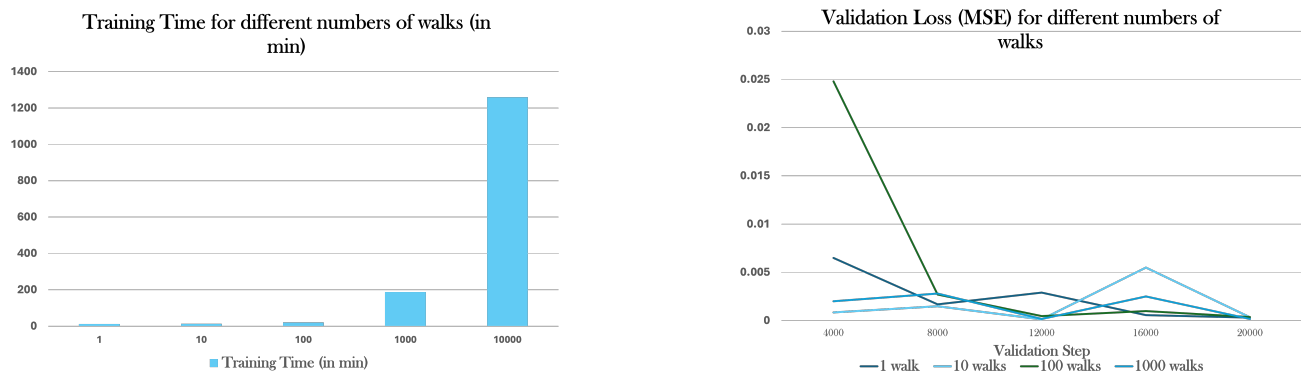


Figure 7. **Left:** This figure showcases the overall training time as the number of trajectories changes for each instance. The higher number of trajectories increases the training time due to a higher likelihood of longer random walks. **Right:** This plot shows comparable performance for different numbers of walks for each instance. Asymptotically, neural operators converge to a similar level of errors regardless of the fidelity of the stochastic estimation.